

## Megacam: A Wide-Field CCD Imager for the MMT and Magellan

BRIAN MCLEOD, JOHN GEARY, MAUREEN CONROY, DANIEL FABRICANT, MARK ORDWAY, ANDREW SZENTGYORGYI,  
STEPHEN AMATO, MATTHEW ASHBY, NELSON CALDWELL, DYLAN CURLEY, THOMAS GAURON, MATTHEW HOLMAN,  
TIMOTHY NORTON, MARIO PIERI, JOHN ROLL, DAVID WEAVER, AND JOSEPH ZAJAC

Harvard-Smithsonian Center for Astrophysics, 60 Garden Street, Cambridge, MA 02138; bmcleod@cfa.harvard.edu

AND

POVILAS PALUNAS AND DAVID OSIP

Las Campanas Observatory, La Serena, Chile

Received 2014 December 18; accepted 2015 January 23; published 2015 March 6

**ABSTRACT.** Megacam is a large-format optical camera that can be operated at the  $f/5$  Cassegrain foci of the MMT on Mount Hopkins, Arizona, and the Magellan Clay telescope at Las Campanas Observatory, Chile. Megacam’s focal plane is composed of 36 closely packed e2v CCD42-90 CCDs, each with  $2048 \times 4608$  pixels, assembled in an  $18,432 \times 18,432$  array. Two additional CCD42-90s are provided for autoguiding and focus control. The CCDs have  $13.5 \mu\text{m}$  square pixels that subtend  $0''.08$  at the  $f/5$  foci, yielding a  $25' \times 25'$  field-of-view. The camera system includes a focal plane shutter, two filter wheels, two liquid nitrogen reservoirs, a central chamber that holds the CCD mosaic array, and two electronics boxes. Megacam is equipped with a variety of broadband and narrow-band filters. Software features include automatic calculation of twilight flat exposure times.

*Online material:* color figures

### 1. INTRODUCTION

Megacam (Fig. 1) is a  $25' \times 25'$  camera for the  $f/5$  Cassegrain foci of the MMT (Fabricant et al. 2004) and Magellan Clay (Szentgyorgyi et al. 2012) telescopes. Megacam, which is equipped with *urgiz* filters and has excellent image quality, has a broad scientific mission as a general-purpose imager. Since commissioning, it has been used for a wide variety of research, including Kuiper Belt objects (Bianco et al. 2009), exoplanet searches (Hartman et al. 2008), characterization of Milky Way satellites (Sand et al. 2014), and weak lensing (Israel et al. 2012).

Megacam is one of a progression of back-illuminated mosaic CCD cameras that began nearly 20 years ago with the Big Throughput Camera (Wittman et al. 1998) at Cerro Tololo. The Sloan Digital Sky Survey camera (Rockosi et al. 2002) was the first to contain dozens of CCDs. The MMT and Magellan Megacam is in many senses a twin of the CFHT MegaCam (Boulade et al. 2003). Though designed and built completely independently, it ended up with the same quantity of the same CCDs, with nearly identical filters, and the same name.

Subaru, first with Suprime-Cam (Miyazaki et al. 2002), and now Hyper Suprime-Cam (Miyazaki et al. 2006), is the largest telescope with a big mosaic camera. The gigapixel PanSTARRS camera (Onaka et al. 2012) is the largest operating focal plane. The latest generation of mosaic cameras, including DECam (Flaugher et al. 2012) and Hyper Suprime-Cam take advantage of the enhanced red response and reduced fringing offered by

deep depletion CCDs, as will the Large Synoptic Survey Telescope camera (Kahn et al. 2010).

The MMT and Magellan Megacam, though not the largest mosaic or on the largest telescope, remains highly competitive due to its excellent blue efficiency and extremely good image quality, with  $0''.32$  images observed across the full field-of-view. In this article, we give a comprehensive description of the instrument, data reduction methods, performance, and selected scientific highlights. Key parameters of the instrument are given in Table 1.

#### 1.1. Instrument Overview

A cutaway view of Megacam is shown in Figure 2. The instrument is constructed in two sections. The upper section, or “top box,” contains the shutter, filters, and, at Magellan, a wave-front sensor. The lower cryostat contains the CCD focal plane and is cooled with liquid nitrogen ( $\text{LN}_2$ ). Each section has its own electronics.

The heart of Megacam is the focal plane, which is comprised of 36 CCD42-90 CCDs manufactured by e2v, each with  $2048 \times 4608$  pixels, and mosaicked into an  $18,432 \times 18,432$  pixel array. The CCDs are closely packed on all four sides with gaps subtending  $6'$  or  $31'$  as shown in Figure 3.

Megacam is fed by the  $f/5$  configuration of either the MMT or Magellan Clay 6.5 m telescopes, which have identical refractive correctors. Megacam is equipped with a standard set of

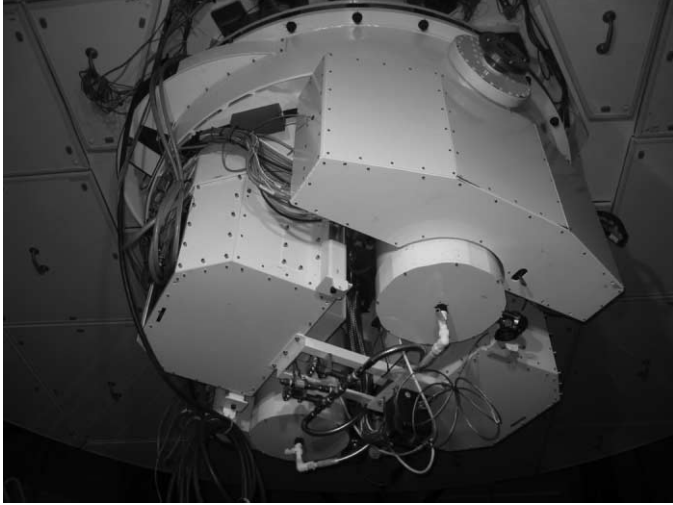


FIG. 1.—Megacam installed on the Magellan Clay Telescope. Visible are the two cylindrical liquid nitrogen cryostats, CCD electronics (*right and left*), and ancillary electronics (*top*).

*ugriz* filters. Individual investigators have also acquired project-specific broadband and narrowband filters.

Megacam was commissioned in November 2003 at the MMT, and placed into routine scientific operation in 2004. It was recommissioned at the  $f/5$  focus of the Magellan Clay Telescope in October 2009, where it has been in routine scientific operation since 2010. The Magellan deployment included a new filter wheel, shutter, and wavefront sensor housing, while the cryostat, CCDs, and CCD electronics were shipped from the MMT.

## 2. CCDS

### 2.1. CCD Characteristics

The CCDs have  $13.5 \mu\text{m}^2$  pixels that subtend  $0''.08$  at the  $f/5$  focus, yielding a field-of-view of  $25' \times 25'$ . We achieve a system read noise of  $5 e^-$  with a 145 kHz pixel rate using the electronics described below. The CCDs have a broadband AR coating, and their quantum efficiency is shown in Figure 4. The Invar CCD package contains shims that were lapped by e2v so that each CCD's surface is  $14.000 \pm 0.0125$  mm above the mounting surface. With this metrology provided by the manufacturer, we did not perform additional metrology or adjustment of the assembled focal plane surface. The CCDs are each flat to better than  $5 \mu\text{m}$ .

### 2.2. CCD Mounting and Installation

The CCD42-90 packages and installation procedure were designed in collaboration with manufacturer e2v with the goal of allowing safe installation in a closely packed configuration. The CCD packages have three M3 threaded studs that protrude from the bottom of the package. These studs are used to secure the

TABLE 1  
BASIC PROPERTIES OF MEGACAM

Item	Value
Number of CCDs	36
CCD type	e2v CCD42-90 back-illuminated
CCD layout	$9 \times 4$ array
Pixels per CCD	$2048 \times 4608$
Pixel size	$13.5 \mu\text{m}$
Field-of-View	
Total	$25' \times 25'$
Single CCD	$160'' \times 360''$
Plate scale	$0.169 \text{ mm arcsec}^{-1}$
Pixel scale (binned $\times 2$ )	$0.16 \text{ arcsec pixel}^{-1}$
CCD gap size	
Small	$6'$
Large	$31'$
Exposure Overhead	
Readout time (single amp, binned $2 \times 2$ )	$22 \text{ s}$
Additional (file write, shutter, etc.)	$15 \text{ s}$
Guide-star lock (typical)	$2\text{--}10 \text{ s}$
Total	$\sim 45 \text{ s}$
Digitization	16 bit (65,536 ADU)
Gain	$3.5 e^- \text{ ADU}^{-1}$
Read noise	$5 e^-$
FITS file size (binned $2 \times 2$ )	$184,345,920 \text{ bytes}$
Standard filters	$u, g, r, i, z$
Typical QE	$55\% @ 350 \text{ nm}, 82\% @ 500 \text{ nm}, 30\% @ 900 \text{ nm}$

device to the cold plate and are also used to provide crude lateral placement during the installation. The final lateral position is constrained by two precision pins that also protrude from the bottom of the device package. During installation, as illustrated in Figure 5, the device is held by a rod that is inserted through the cold plate and then threaded into the bottom of the CCD package. The device is raised into position using this handling rod. A shorter rod also threaded into the package ensures that the device is clocked correctly before it gets close to the focal plane.

## 3. OPTICS

### 3.1. Telescope and Corrector Optics

The  $f/5$  optics at the MMT and Magellan Clay telescopes are essentially identical and are comprised of the 6.5 m diameter parabolic primary mirror and a 1.8 m diameter hyperbolic secondary mirror. To correct the inherent coma in the Cassegrain optics, a four-element, all-fused-silica refractive corrector is used (see Fig. 6). The corrector consists of three lenses located just behind the primary mirror vertex, as well as a final lens located just before the focal plane. This final 48-mm-thick element serves a dual role as a field-flattener and as the window to the cryostat. The optical prescription is given by Fabricant et al. (2004). The

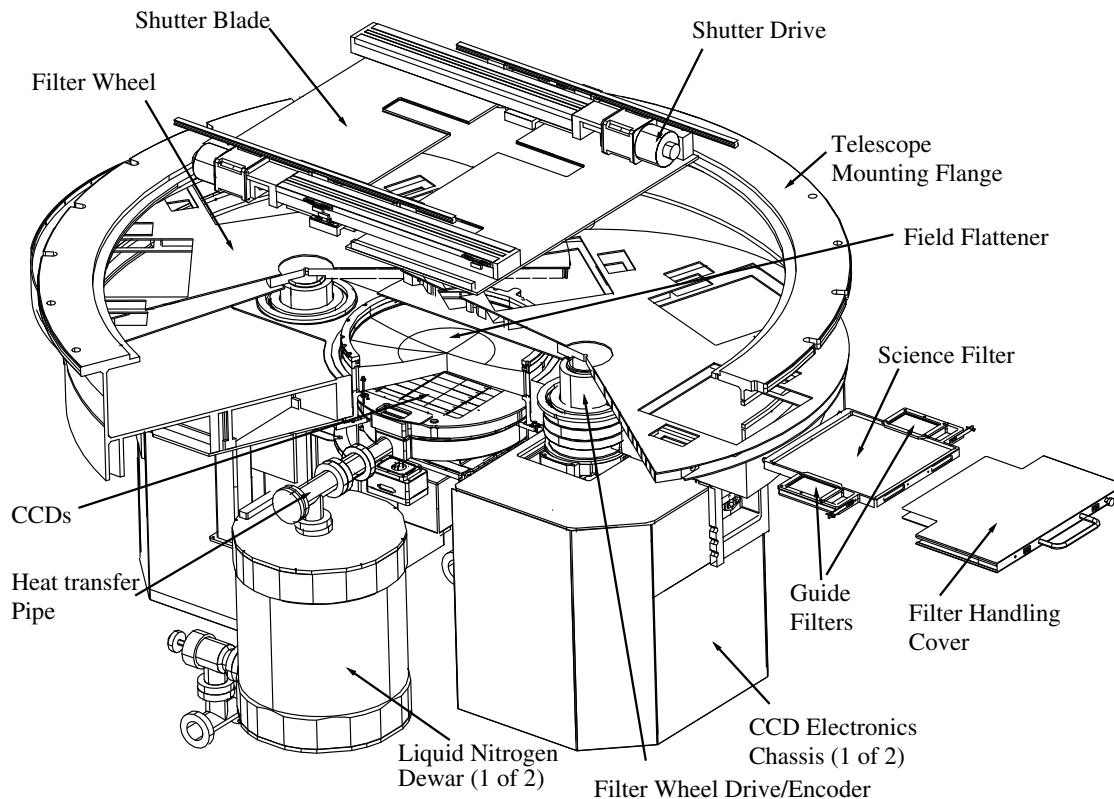


FIG. 2.—Cutaway view of the instrument.

optical design yields images with  $0''.06$  to  $0''.16$  FWHM, depending on the wavelength and field position (see Fig. 7).

The two sets of three corrector lenses were fabricated by Goodrich Optical Systems and were AR coated with solgel by Cleveland Crystals. The field-flattener window was fabricated by Harold Johnson Optical Labs and AR coated with a hard multilayer coating by Sagem.

The native pixel size is  $0''.08$ , a product of the  $f/5$  focal plane scale and the  $13.5\ \mu\text{m}$  physical pixel size that was available as an item of commerce when the CCDs were purchased. Any advantage gained by reimaging to a coarser scale would have been outweighed by poorer image quality and a large, complex, and expensive optical system. Because there is no performance penalty, we normally bin the pixels by two except during conditions of exceptional seeing.

### 3.2. Filters

Megacam's filters were fabricated by Sagem. We purchased one *ugriz* set for the MMT and a second set for Magellan. In the MMT set, each filter is constructed from two  $300\ \text{mm}^2$  substrates, each 5 mm thick. Typically, one substrate is made from colored Schott glass and serves as a blocking filter, while the other substrate defines the bandpass with interference coatings. The two layers of the filter are not epoxied together.

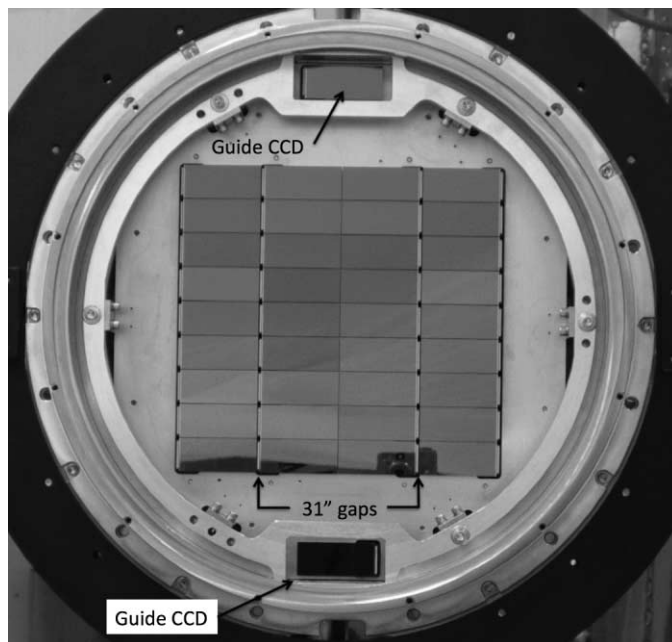


FIG. 3.—The Megacam focal plane. Gaps between the CCDs are 6", except as indicated.

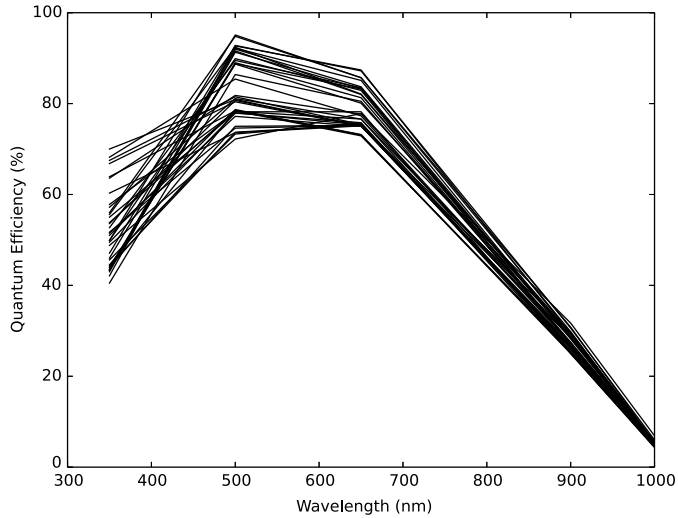


FIG. 4.—Quantum efficiency of the Megacam CCDs, as reported by the manufacturer, e2v.

After the MMT filters were manufactured, some of the Schott colored glasses were discontinued in these large sizes. Thus, with the exception of the *u*-filter, the Magellan set was constructed purely with interference coatings. The *u* filter is on two substrates; the remainder on a single 5-mm-thick substrate.

The 1 kg filter pieces are spring loaded in steel frames with flexures (Fig. 8). Three axial flexures provide a total of 10 g (10 N) restraint. Laterally, 5 g of force is applied through two flexures in one axis, and through one flexure in the other. The filter frame is handled inside a cover that is removed only after the filter is secured within the filter wheel.

A number of additional filters have been purchased by individual investigators for use with their projects. These include a wideband *g+r* filter, and narrowband filters at 393, 410, and 915 nm.

### 3.3. Guiding and Wavefront Sensing

The Megacam focal plane contains two additional CCD42-90 CCDs, which are used for autoguiding and control of the telescope focus. These two CCDs are driven by a separate controller of the same design as the science camera controller. A Shack–Hartmann wavefront sensor is deployed periodically on-axis to measure higher-order aberrations. The arrangement is shown in Figure 9.

### 3.4. Baffles

Though not technically a part of the instrument, the telescope baffles (Fig. 10) are critical to the successful operation of Megacam and so merit some discussion. The goals of the baffles are

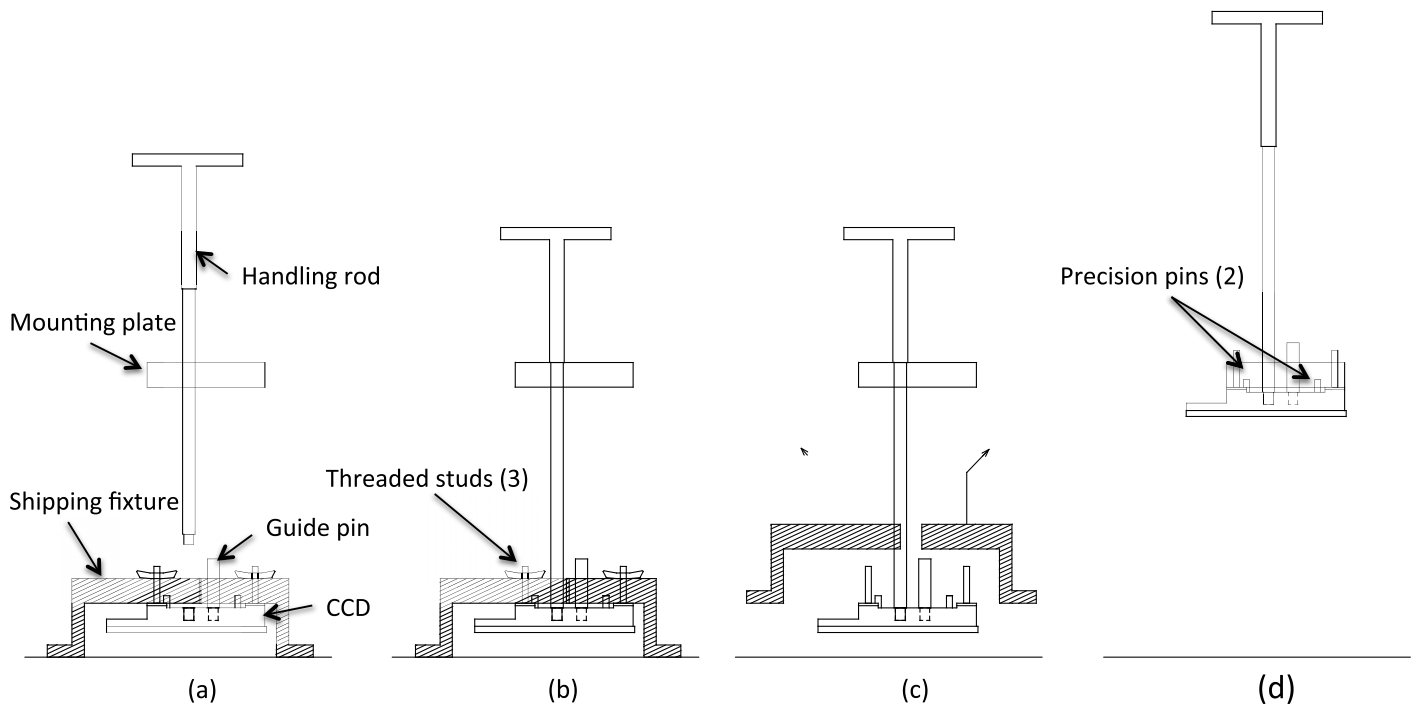


FIG. 5.—CCD installation procedure. The procedure begins with the mounting plate held in a fixture above the table top. (a) The CCD in its shipping fixture is placed below the mounting plate. The guide pin is installed into the CCD. The handling rod is inserted through a hole in the mounting plate and threaded into the CCD. (b) Nuts are removed from the three threaded studs. (c) The shipping fixture is lifted away. (d) The CCD is lifted by the handling rod. The guide pin, threaded studs, and precision pins sequentially engage into the mounting plate. Nuts are installed on the threaded studs. Finally, the handling rod and guide pin are removed, completing the installation.

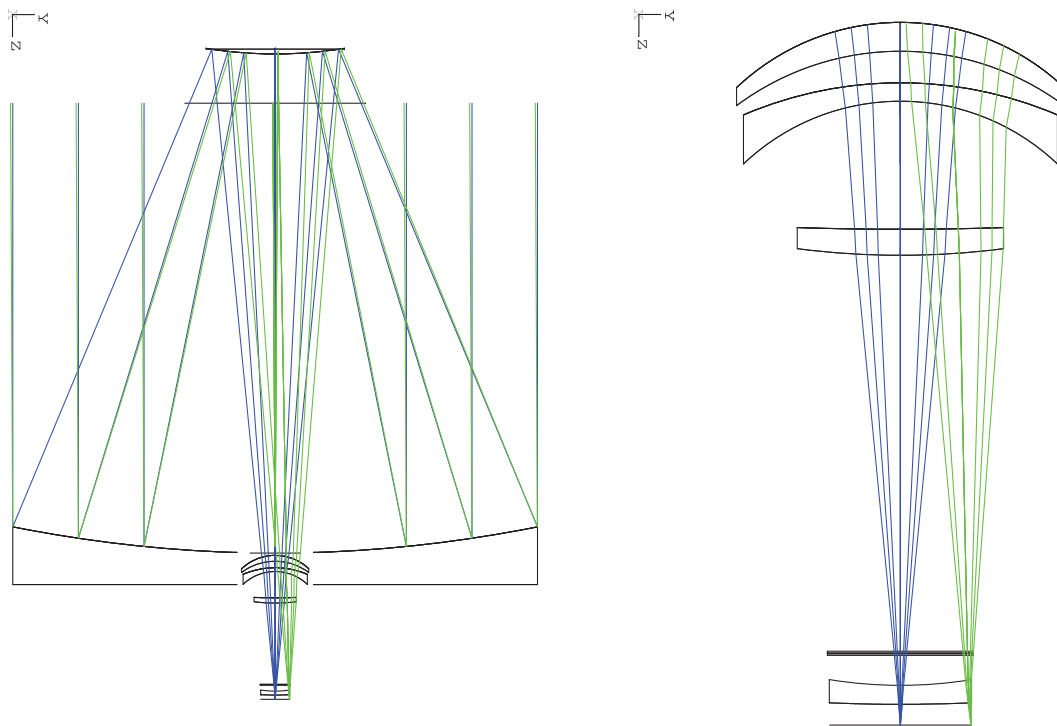


FIG. 6.—MMT and Magellan optical layout, including the 6.5 m diameter primary and 1.8 m secondary mirrors (*left*), and closeup of three corrector elements, filter, and the final field-flattening corrector element (*right*). The largest corrector element diameter is 0.83 m. See the online edition of the *PASP* for a color version of this figure.

fourfold: (1) to prevent direct skylight from reaching the focal plane; (2) to prevent light reaching the focal plane from a single reflection off a baffle surface; (3) to prevent scattered light entering the focal plane from areas outside the primary mirror; and (4) to prevent double reflections on M1 and M2 from reaching the focal plane. Item (3) is a concern for open-tube wide-field telescopes, while item (4) can be a concern for wide-field telescopes that have an M1 hole diameter smaller than M2. A set of critical baffles would normally include a very large M2 baffle and an M1 baffle extending from the M1 vertex. Mechanical constraints, however, at each of the telescopes prevented us from making nominal baffles.

At the MMT, the roll-up mirror cover does not allow a permanent structure to extend more than 1 m above the M1 vertex. This drove us to design a “midbaffle” that is attached to the telescope structure only by guy-wires and which does not extend completely to M1 itself. To lessen wind-loading, the midbaffle was made of a set of rings instead of a single cylinder. This midbaffle, however, allows large-angle light to reflect off M1, off M2, go inside the midbaffle, and reflect off M1 again, M2 again, and then arrive at the focal plane. This double-bounce problem was solved by placing an appropriately sized obscuring disk at the center of M2. Details of the mechanical design and construction of the MMT baffles are provided by Callahan et al. (2008).

The Magellan mirror cover design led to three baffles, a short cylindrical M1 baffle, a ringed midbaffle, and a cylindrical M2

baffle. Double-bounce light for this telescope was eliminated by a large flange at the top of the M1 baffle.

The placement of the rings on the baffles was determined by demanding two scatterings of direct skylight before reaching the focal plane. All surfaces were covered with black flocking material, from Boston Felt, for minimum reflectivity.

## 4. MECHANICAL DESIGN

### 4.1. Topbox housing

The topbox housing is constructed of steel to match the telescope and attaches to the telescope rotator on a 1.829 m diameter bolt circle. Mounted within this housing are the filter wheels, the shutter, and the wavefront sensor (at Magellan only). The bottom surface of the housing contains a precision mounting surface for the cryostat. The top surface contains precision-machined surfaces for maintaining axial and radial positioning relative to the telescope.

### 4.2. Shutter

The shutter is a dual-blade, focal plane curtain-style shutter designed to give excellent exposure time control and uniformity. Each blade is 6.35 mm aluminum plate and travels on rails manufactured by THK, driven from one side by a ball screw and a

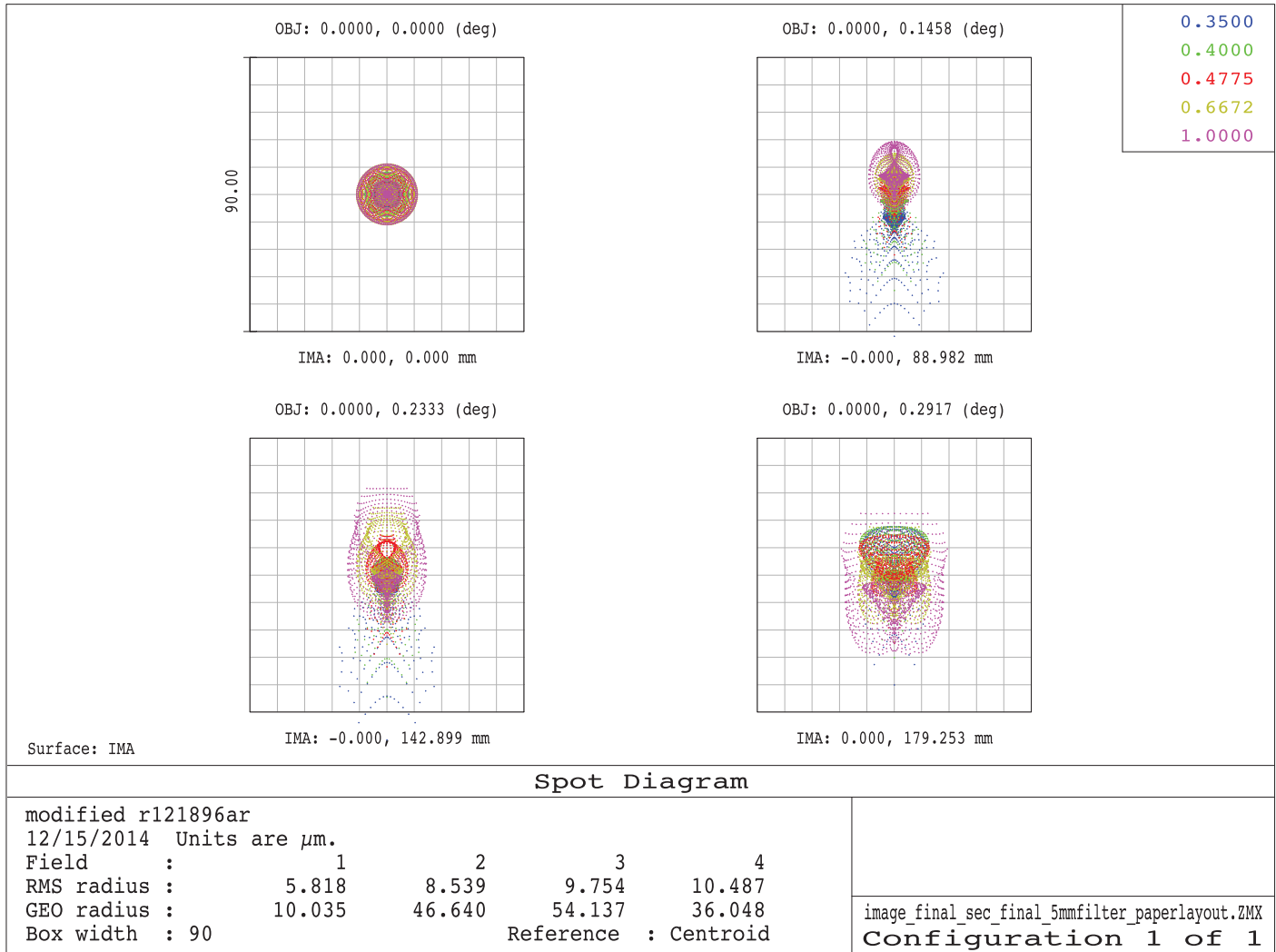


FIG. 7.—Polychromatic spot diagram for Megacam. Each box is 0.75 square. See the online edition of the *PASP* for a color version of this figure.

servo motor. The other side of the blade is attached to the rail with a shoulder screw in a slot to avoid binding due to differential expansion between the aluminum blade and the steel structure. It takes 0.5 s for a blade to traverse the focal plane, and the exposure time is accurate to 1% for a 1 s exposure.

#### 4.3. Filter Wheels

There are two filter wheels, each with five slots. Each wheel consists of two 1.6 mm thick facesheets separated by a 25.4 mm thick steel structure. The wheels are driven from a central hub through a harmonic drive with a servo motor. Next to each wheel is a barcode reader that is used to identify the filters at instrument startup. The barcode readers are turned off during instrument operation. The barcodes are printed on regular paper and taped onto the filter frames.

#### 4.4. Dewar

The  $\text{LN}_2$  CCD cryostat is constructed in three sections that are connected with vacuum bellows. Two aluminum Infrared Laboratories ND-14 dewars flank a central steel chamber containing the focal plane. The 36 science CCDs and two guider CCDs are mounted on an Invar plate. We initially planned to use molybdenum for the plate because its thermal conductivity is several times higher than Invar. Unfortunately the plate arrived from the manufacturer cracked into two pieces. We then switched to Invar, which is less brittle, and have been very happy with that choice.

Heat is extracted from the bottom of the focal plane via copper straps to a set of copper bars which connect to the  $\text{LN}_2$  vessels. We trimmed the copper straps so that the temperature variations are about 15° C across the focal plane. A second round of trimming could have improved these variations, but was omitted as

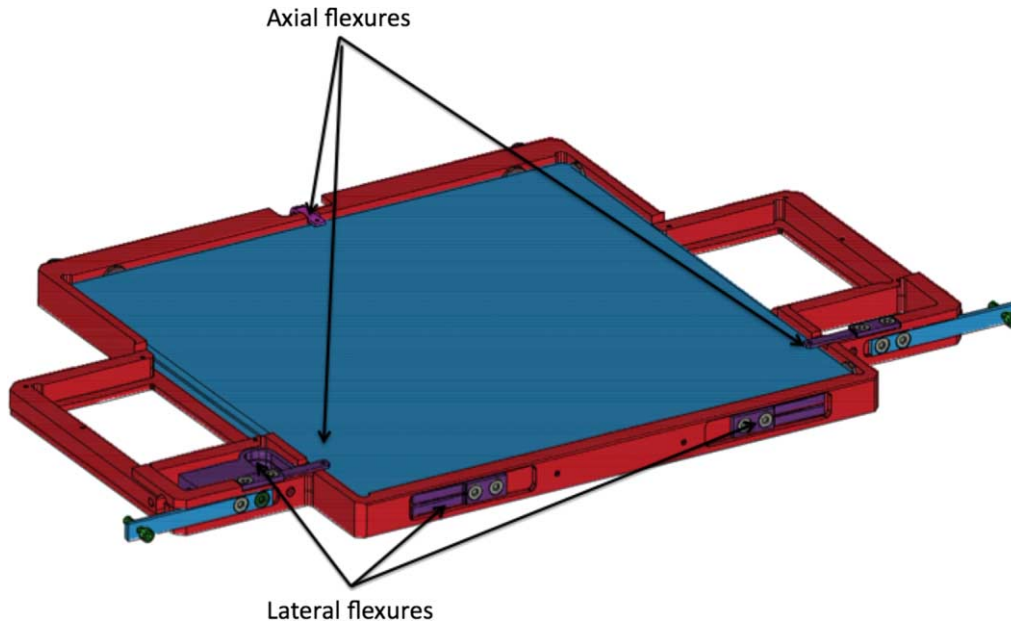


FIG. 8.—Filter frame, showing location of flexures. The guide filters are located to the right and left of the science filter. See the online edition of the *PASP* for a color version of this figure.

we detected no lab performance difference between the warmer and the colder CCDs. Likewise, on sky we have seen no difference in data quality among the CCDs. The temperatures are measured with YSI44001A thermistors which were epoxied into the Invar CCD packages by the CCD manufacturer. A set of resistors distributed across the focal plane allows the temperature to be stabilized. One CCD near the center of the focal plane is chosen to provide the thermal setpoint at  $-115^{\circ}\text{C}$ , with the others stable at temperatures between  $-130$  and  $-115^{\circ}\text{C}$ .

The plate is supported by six Ti6Al4V titanium flexures. Our analysis showed that titanium provided the optimal stiffness to thermal conductivity ratio. The other candidates we considered were stainless steel and an aluminum/G-10 combination.

The calculated thermal load on the CCD focal plane is approximately 37W, with 28W from thermal radiation from the window, 3W conducted through the flexures, and 6W through the flex cables. An additional 4W is dissipated directly into the  $\text{LN}_2$  dewars. The total thermal load was verified by measuring the  $\text{LN}_2$  consumption.

The  $\text{LN}_2$  dewars are filled from the bottom via the standard Infrared Labs inverted fill tubes. We use tubes that extend only 60% the height of the  $\text{LN}_2$  vessel to minimize the amount of  $\text{LN}_2$  that is spilled when the telescope is pointed off the zenith. The hold time with the vessels filled 60% is approximately 36 hr, allowing the instrument to operate with just one fill per day.

#### 4.5. Field-flattener Mounting

The fused silica field-flattener lens is bonded into a stainless steel bezel with a continuous ring of GE RTV560, which maintains window centration and minimizes thermally induced stress

(Fata & Fabricant 1998). With a 48 mm center thickness, the lens has a computed maximum pressure-induced stress of 2.7 MPa, meeting our goal of no more than 3.4 MPa. The bottom concave surface of the lens includes a 6 mm wide polished flat surface at the outer edge that is contacted by a Viton O-ring vacuum seal to the cryostat.

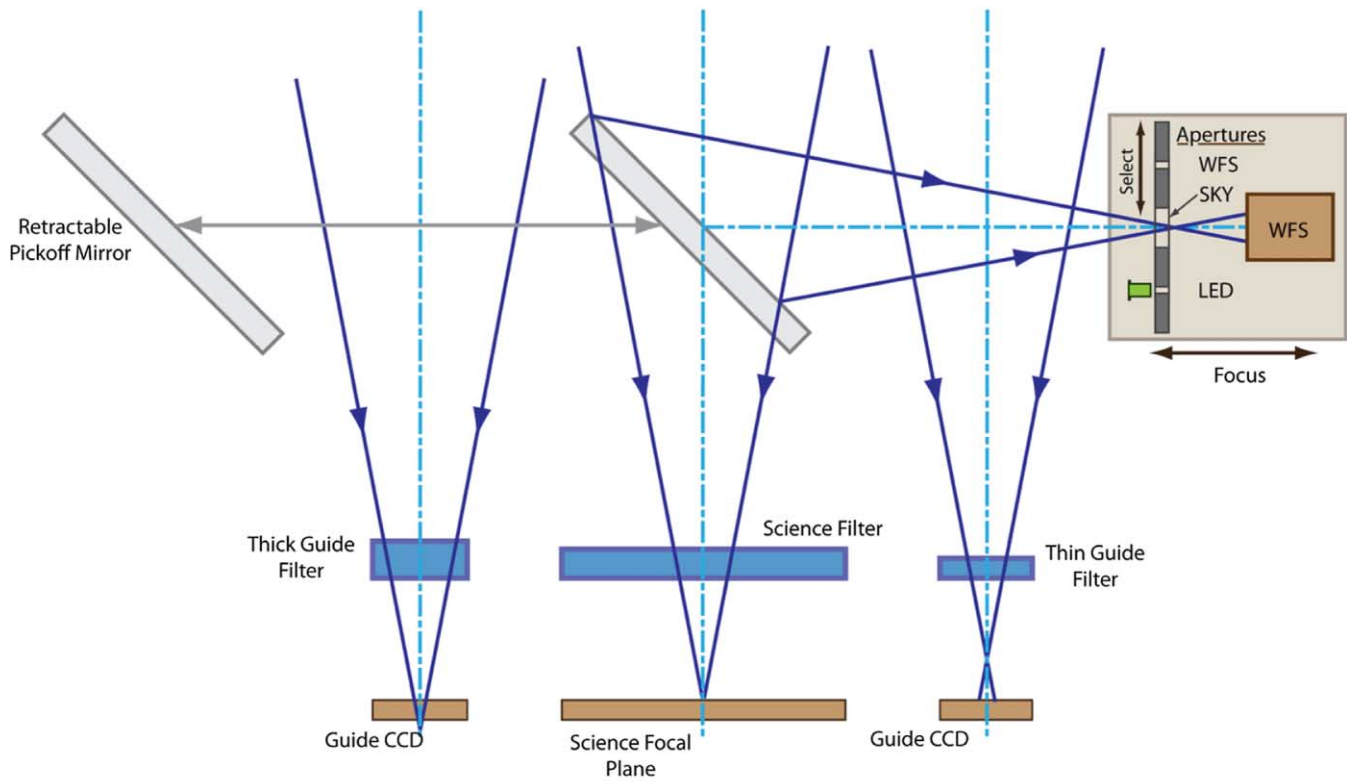
## 5. ELECTRONICS AND DETECTORS

### 5.1. Mechanism Control

The mechanisms in Megacam are driven by DC servo motors and a DeltaTau PMAC motion controller. At the MMT, the VME-based PMAC controller and associated Copley servo drives are in a rack located off the telescope. This requires a 10 cm diameter bundle of cables to operate the instrument. At Magellan, the newer compact-PCI PMAC controller and all servo drives were put in an electronics box located on the instrument housing. Only power and Ethernet are required to be provided to the instrument in this model.

### 5.2. CCD Controller

The CCD controller, designed and built at SAO, is divided into two chassis, known as the “master” and “slave,” each responsible for half of the CCDs. Each chassis contains 9 four-channel video processing cards, 6 three-CCD driver cards, and 1 driver/receiver card which sends commands and data to the other chassis over a 16-bit parallel bus. In addition, the master side contains a timing generator card and an I/O communications card. Command and data communications to a Linux data acquisition computer are via an EDT PCX-RCX fiber interface.



### Megacam - Magellan Guide/Wavefront Sensor (WFS) System

FIG. 9.—Schematic representation of the science CCDs, guider CCDs, and wavefront sensor. See the online edition of the *PASP* for a color version of this figure.

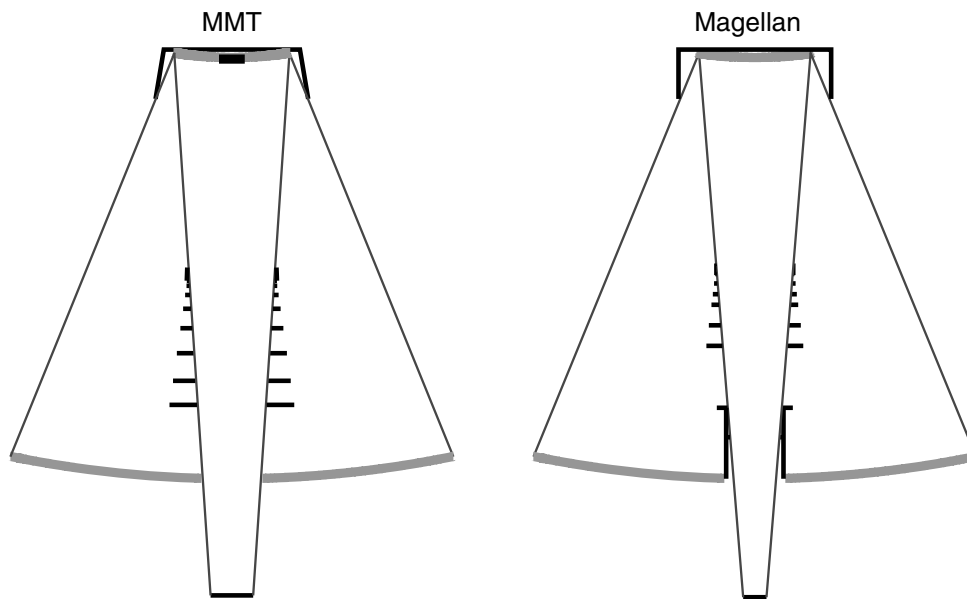


FIG. 10.—Telescope baffles for the MMT and Magellan f/5 configurations.



The boards in each chassis are connected together with a custom 6U VME-style backplane. Further details on the controller can be found in McLeod et al. (2006).

### 5.3. CCD Electrical Connections

Electrical connections to the CCDs are made from the bottom of the CCD package via a custom zero-insertion-force (ZIF) socket manufactured by Tactic Electronics and provided by e2v as part of the CCD procurement. A soldered flexible printed circuit provides the connection between the ZIF sockets and 55-pin circular hermetic connectors. Three CCDs (six video channels) are connected to each hermetic connector. These flex circuits provide low-pass R-C filtering of critical bias voltages as well as static-protection diodes on all leads. By using thin copper traces for the signals, and a serpentine interlaced ground plane layer, good thermal standoff between the warm hermetic connectors and the cold ZIF sockets was achieved.

Because of space constraints, it was not possible to use standard mating connectors on the outside of the hermetics, so connections were made via a short two-inch cable, soldered directly to the hermetic pins, running to a pair of Positronic SGM-series 26-pin connectors. Each Positronic pair mates to a six-channel preamplifier board, which in turn plugs directly into a 50-pin D-connector on the controller backplane.

### 5.4. CCD Operation

The CCDs are operated with a conversion gain of  $3.5 e^- \text{ADU}^{-1}$  at a 145 kHz pixel clock rate. The data can be read out of either one or two amplifiers per CCD which, after including prescan and overscan pixels, yields a readout time of 69 or 37 s when unbinned, or a readout time of 22 or 12 s when binned by a factor of 2. Due to one data channel with intermittently high noise, we operate in single-amplifier mode, except for those projects with large numbers of short exposures when minimizing overhead is paramount. We use the bias voltages recommended on each CCD's manufacturer-supplied data sheet. No channel-to-channel crosstalk has been detected to a limit of  $10^{-5}$ .

### 5.5. Window Thermal Control

The dewar window cools radiatively to the cold focal plane below, resulting in a central temperature that is measured to be  $6^\circ \text{C}$  lower than the outer edge. We apply 30 W of resistive heating to the window bezel, which keeps the bezel from dropping below ambient temperature. In addition, we blow dry air into the space just above the window to prevent condensation from forming on the window. When the cold instrument needs to be unplugged for lightning protection or during transport inside the observatory, a 12 V rechargeable battery pack provides power for the heaters.

## 6. OBSERVING WITH MEGACAM

In this section, we describe the observing procedures for Megacam. Some steps are performed only once at the beginning of each two-week observing run, including the measurement and correction of field-dependent astigmatism due to miscollimation of the telescope. Once per run, we also make dithered observations of a star field for determining illumination and astrometric corrections, as discussed in detail in § 7.4.6. Flat-field data are collected nightly in either evening or morning twilight. A typical Megacam observation begins with slewing the telescope to a star near the intended science target, where the telescope is collimated to eliminate coma. Then the telescope is slewed to the target, where guide stars are acquired and the guiding and focus control is activated. Finally, the Megacam exposure sequence is started.

### 6.1. Flat-Fielding

The telescope enclosures are located a short distance from the upper end of the telescopes, making it very difficult to evenly illuminate a flat-field screen. For that reason, we rely exclusively on twilight flat fields. We typically take twilight flats at elevation angle  $80^\circ$  with the azimuth in the antisolar direction, where we expect the gradient in the sky brightness to be small. Sometimes this location is in the Galactic plane, which forces us to choose an alternate location.

We compute the twilight flat exposure times automatically based on a simple empirical model of the detected flux from the sky ( $I$ ) versus angle ( $\alpha$ ) of the sun below the horizon in degrees ( $\alpha$  is negative). The relation is  $I = 10^{c_1 + c_2 \alpha}$ . The constants  $c_1 \{\log_{10}[e^- \text{s}^{-1} \text{m}^{-2} \text{arcsec}^{-2}]\}$  and  $c_2$  that we have adopted at Magellan are shown in Table 2. We aim to have 20,000 ADU ( $70,000 e^-$ )  $\text{pixel}^{-1}$ , which is well exposed but still well within the linear regime. After the first exposure, we correct the exposure time based on the observed number of counts in the previous exposure. The counts in the first exposure may vary by a factor of 2 from night to night, but by using the correction factor, all subsequent exposures are within a few percent of the target level. Using this automated mode, it is possible to take 25 perfectly exposed flat fields during the twilight period.

### 6.2. Telescope Collimation

A wide-field telescope must be collimated to eliminate both coma and off-axis astigmatism. The coma, which is made constant over the field-of-view by the refractive corrector, is removed by rotating the secondary mirror about the pointing-neutral location based on the Shack–Hartmann measurements described in the next section. This will leave a field dependent astigmatism pattern (McLeod 1996).

To measure and correct the astigmatism, we take Megacam images of a star field defocussed to an image diameter of  $3''.5$ . The stars are identified using SExtractor (Bertin & Arnouts

TABLE 2  
TWILIGHT SKY BRIGHTNESS COEFFICIENTS

Filter	$c_1$	$c_2$
<i>u</i>	4.88	0.50
<i>g</i>	5.50	0.476
<i>r</i>	5.40	0.476
<i>i</i>	5.72	0.509
<i>z</i>	4.84	0.455

1996). For each star, we then use a contour plotting algorithm to identify the 50% flux contour, and then fit an ellipse to that contour. Then we compute a least squares solution to determine the “zero-coma tilt” of the secondary mirror that would produce the observed pattern of ellipticities vs position in the field. In practice, we have found it sufficient to measure the astigmatism pattern at the beginning of an observing run, and then rely on an open-loop lookup flexure model to maintain the alignment after that.

### 6.3. On-Axis Wavefront Sensor

Telescope aberrations, including coma due to miscollimation and aberrations due to gravity and thermal deformation of the primary mirror, are corrected periodically on-axis using a Shack–Hartmann wavefront sensor. These measurements are typically made once an hour or at the start of each new target. At the MMT, we use the facility  $f/5$  wavefront sensor (Pickering et al. 2004). At Magellan, the wavefront sensor is integral to Megacam, but is fed into the facility analysis system (Schechter et al. 2003). The residual aberrations measured by the wavefront sensor introduce a  $0''.11$  contribution to the FWHM.

### 6.4. Guide-Star Selection

Guide stars are chosen automatically from the GSC2 catalog (Lasker et al. 2008) whenever the telescope is pointed or offset. The guider CCD controller is programmed to read out a  $12''$  window from the fixed guider CCD. Guider images are taken once a second with an exposure time of 0.5 s. If the automatically chosen star turns out to be inappropriate (e.g., too close to another bright star, or actually a galaxy), the telescope operator may choose a different one from a star map representation of the guide camera’s field-of-view. When the telescope is moved a small amount, the same guide star is used if possible. Nonsidereal tracking of solar system objects is also possible with the guide box location updated in real time as the telescope tracks.

### 6.5. Focus Control

The two guider CCDs look out through their own filters, with one thicker and one thinner than the science filter. The thickness is chosen to cause them to be out of focus by plus and minus  $0''.5$  image diameter. When the telescope focus changes, one image

gets smaller while the other gets larger. The longitudinal defocus at the focal plane is given by

$$dz = \frac{f^2(F_1^2 - F_2^2) - (d_1^2 - d_2^2)}{2(d_1 - d_2)}, \quad (1)$$

where  $f$  is the focal ratio,  $F_i$  is the FWHM of image  $i$ , and  $d_i$  is the effective displacement from the nominal focal plane for image  $i$ . The effective displacement is given by  $d_i = \sum_j t_{ij}(1 - 1/N_{ij}) - \sum_j t_{sj}(1 - 1/N_{sj})$ , where  $ij$  and  $sj$  refer to layer  $j$  of guide filter  $i$  or the science filter. The focus correction is made every 10 guide frames to average out the effects of seeing.

### 6.6. Continuous Readout Mode

To conduct a search for transiting Kuiper Belt objects, we implemented a continuous readout mode for Megacam. We open the shutter and then read out the detector continuously. The star images then become continuous trails with the vertical axis becoming the time axis. We record data for 15 minutes at a stretch before closing the files and starting again. The analysis of this data, described in detail by Bianco et al. (2009), turned out to be quite challenging because not only do the star trails overlap each other, any star motion in the vertical transfer axis appears as an intensity variation.

## 7. SOFTWARE

### 7.1. Overview

The Megacam software system supports both night-time observing and pipeline data reduction. The majority of the Megacam observing software is written in Tcl with some low-level code written in C. The systems client/ server architecture is implemented using a simple protocol sending ASCII messages over TCP sockets (Roll & Mandel 2001). Typically, one server application controls each hardware subsystem. Server commands expose the hardware functions to the user interface and to script clients that are used to operate the instrument. To minimize external dependencies, all interfaces with the Magellan or MMT facilities are localized in a single site-specific telescope server component.

### 7.2. Observer Interface

Megacam is controlled with a GUI (Fig. 11) that lets the observer take exposures, either one at a time or in a sequence driven by a catalog of exposure properties. In manual mode, the observer selects the filter, exposure time, and dither position relative to the current telescope position. After pressing the “Go” button, the exposure is taken. More commonly, the observer will select a catalog which specifies a sequence, with filter changes, varying exposure times, and dither positions carried out in sequence. As long as one is dithering less than  $1^\circ$  from the

nominal pointing direction, the data taking can be fully automated with new guide stars selected automatically as necessary.

The user interface communicates via the ASCII message protocol to a translation layer that uses the IRAF Control Environment (Schaller 1990) protocol to send commands to the detector server. The multithreaded detector server writes the data directly to disk asynchronously to achieve the necessary data rate.

Every exposure is automatically displayed in a ds9 image display window (Joye 2011), which is paired with an IRAF window for quick image-quality analysis. There is a default post-processing procedure that analyzes the point sources and displays the distribution of FWHM values. This on-the-fly analysis allows the observer to determine when the image quality is starting to soften and allows wavefront sensing to be requested. The observer is allowed to provide postprocessing scripts of their own in place of the default processing, e.g., to measure image ellipticities or to record photometric zero points on specific fields.

### 7.3. Data Archive

Two additional copies of the original data are made as each exposure is read out. One copy is automatically placed in a protected archive directory. From there, the images are automatically transferred each day to SAO in Cambridge, Massachusetts, and imported into the telescope master archive. A second copy is provided to the observer for near-real time analysis, while the original copy is maintained for redundancy on the data acquisition computer system.

### 7.4. Data Reduction Pipeline

#### 7.4.1. Overview

The Megacam pipeline is implemented as a sequence of individual steps comprised of custom C programs, publicly available packages, and IRAF tasks. The tasks are sequenced using Unix shell scripts that are driven from a Tcl/Tk graphical user interface (GUI). The GUI allows the operator to select which

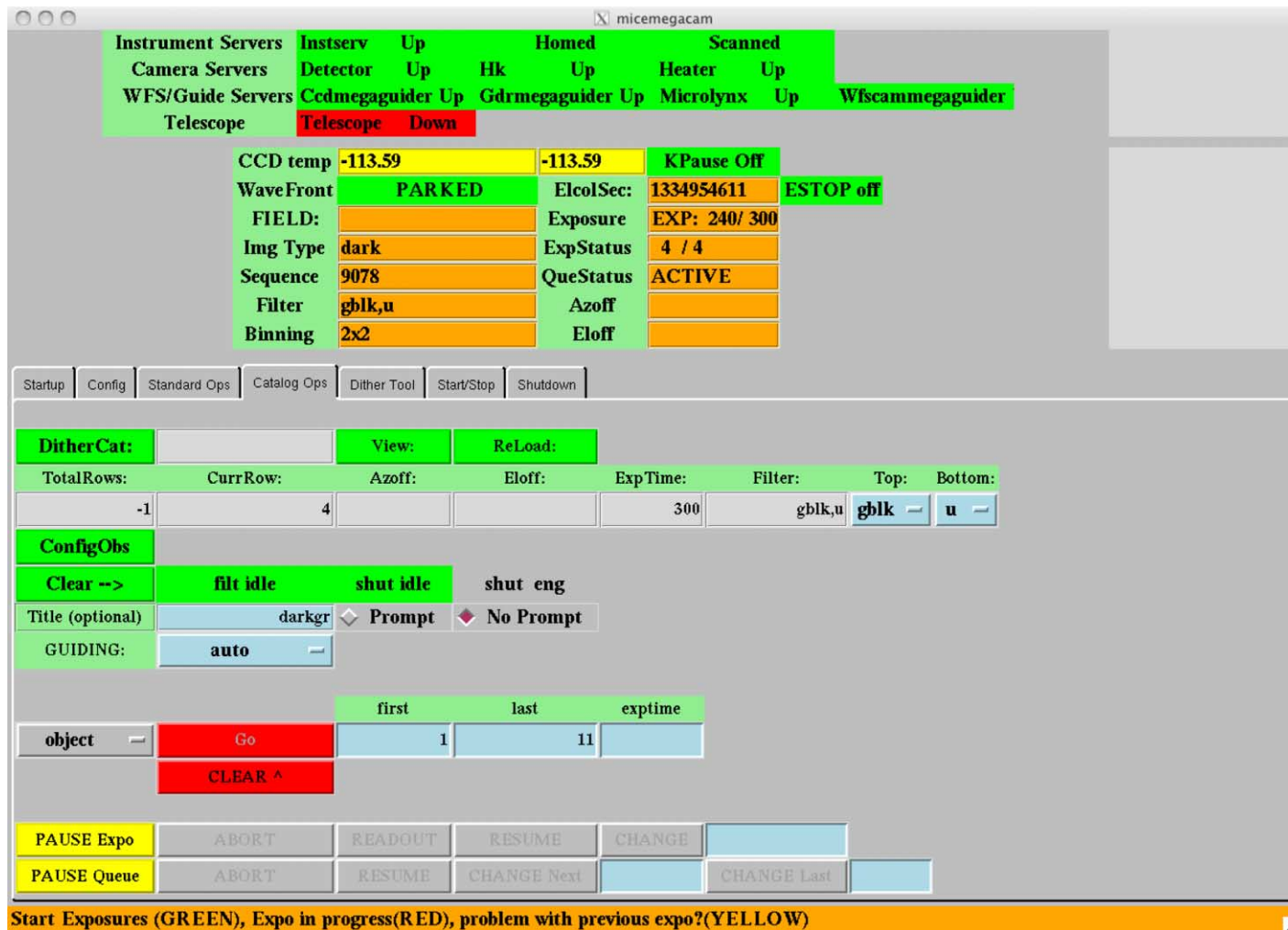


FIG. 11.—Megacam observing graphical user interface. See the online edition of the *PASP* for a color version of this figure.

calibration or science frames are to be processed, which steps of the pipeline are to be run, and the parameters for each step. All the chosen parameters are saved and archived. The pipeline runs on a multicore 64 bit Linux system.

#### 7.4.2. Overscan, Bias, and Dark Correction

The initial steps of the processing are the standard overscan, bias, and dark corrections which are implemented using the IRAF `ccdproc` task. Overscan correction is done on a line-by-line basis, which allows a slight temporal instability in the bias level to be removed.

#### 7.4.3. Flat-fielding

As described above, flat fields are constructed from twilight frames. Typically, five or more exposures are taken in each filter. These exposures are median combined, and then applied to the flat-field frames themselves. This allows detection and masking of stars in the flat-field frames. The frames are again median combined, with the mask applied.

#### 7.4.4. Cosmic Ray Rejection

Cosmic ray rejection is performed using the “lacosmic” routine in IRAF (van Dokkum 2001). Masks of rejected pixels are maintained for exclusion from the final stacked field images, but are temporarily filled with a local intensity estimate to allow usual statistical values to be computed for background estimates.

#### 7.4.5. Defringing

The Megacam CCDs exhibit noticeable fringing at  $i$  and  $z$  bands, 1 and 4% rms, respectively. Fringe frames are constructed by iteratively masking stars and median combining the frames.

To apply the fringe frame to each science frame  $I_j$ , a least-squares solution is performed by minimizing  $\sum_{x,y} (I_j - (Ff + Xx + Yy + A))^2$ , where  $f$  is the fringe frame,  $x$  and  $y$  are the position on the detector, and  $F$ ,  $X$ ,  $Y$ , and  $A$  are the scalars to be solved for. The sum is over all pixels  $x$ ,  $y$  in the image that are not masked as stars. The solution is performed multiple times, masking stars after each step. For sparse fields, the algorithm is applied to each CCD independently. For fields with extended objects that fill a significant fraction of a CCD, the entire mosaic is treated as a whole.

#### 7.4.6. Illumination Correction

The purpose of the illumination correction is to modify the intensity scaling of the image on large spatial scales to produce correct photometry. Several factors can contribute to the illumination correction, including optical distortion and gradients in the flat-field frames. The set of calibration images consists of twelve 60 s exposures taken of the same field, but offset in  $(X, Y)$  position by the following amounts (arcseconds):

(0,0), (85,0), (171,0), (342,0) (682,0) (−682,0), (0,85), (0,171), (0,342), (0,682), (0,−682), and (342,342). The brightnesses of all the stars in each exposure are measured with SExtractor. The illumination correction frame is constructed piecewise as a set of linearly varying terms, one for each CCD, i.e., the correction for CCD  $i$  is  $I_i = A_i + X_i x + Y_i y$ , where  $x$  and  $y$  are the pixel coordinates within the CCD. The construction of the illumination frame is a least-squares minimization of  $A_i$ ,  $X_i$ , and  $Y_i$ , so that the measured dispersion of each star magnitude over the various locations that it appears in the 12 exposures is minimized. No external star catalog is required—the illumination frame produces self-consistency so that a star has the same brightness wherever it appears in the Megacam mosaic.

The computed illumination correction is subsequently applied to each flattened and defringed science exposure. The dominant source of variability in the illumination correction is due to variable amounts of gradient in the twilight flats. For this reason, we find that we can reuse the illumination correction raw frames from a previous night, as long as those data are reprocessed using the same flat that will be used on the science frames.

The amplitude of the illumination correction is typically 5% and is dominated by the quadratic radial dependence expected from the optical distortion. Resulting photometric performance is discussed further below.

#### 7.4.7. Astrometric Solution

The astrometric solution is determined assuming a single radial distortion polynomial that maps angular distance from the optical axis to a linear distance in the focal plane. The astrometric solution is determined in two steps. First, the global distortion polynomial and the location of each CCD in the mosaic is determined using the same set of calibration images used for illumination correction. We vary the parameters of this solution to minimize the variance in the reconstructed position of each star that is measured in multiple places in the mosaic. The radially symmetric distortion polynomial is of the form  $\theta = a_1 r + a_3 r^3 + a_5 r^5$ . Once determined, this polynomial is then inverted to the form  $r = s(\theta + PV2_3 \theta^3 + PV2_5 \theta^5)$ , where  $s$  is the pixel scale, and  $\theta$  is in radians. The keywords `PV2_j` are stored in the FITS header in conjunction with the WCS type keywords `CTYPE1=RA-ZPN` and `CTYPE2=DEC-ZPN` (Calabretta & Greisen 2002). The nominal distortion coefficients computed from the optical design are `PV2_3=349.232` and `PV2_5=518173`. As with the illumination correction, determining this solution is done independently of any external star catalog. The mosaic geometry solution is typically performed once per observing run.

Individual mosaic exposures are then registered to an external catalog using the previously determined solution, solving for only six parameters: the right ascension and declination of the center of the image, the scale, the rotation, and the shear vector. These terms are represented in the FITS header with the keywords `CRVAL1`, `CRVAL2`, and the four `CDi_j` terms.

### 7.4.8. Image Combination

The final stage of the pipeline uses SWarp (Bertin et al. 2002) to transform each image in a dithered sequence to a common target center and pixel scale using a tangent plane projection. After reprojection, the images are combined either directly by SWarp or with the IRAF imcombine task. Input weight maps are derived from cosmic ray removal, bad pixel masks, and saturated pixels.

## 8. MEGACAM PERFORMANCE

### 8.1. Band Passes and Throughput

The measured system throughput of Megacam is determined using SDSS stars and is listed in Table 3. To compare with what we should expect, we account for a telescope area of 29 m<sup>2</sup>, atmospheric extinction, two aluminum reflections, eight refractive surfaces, the filter, and manufacture-reported CCD quantum efficiency. The measured values are within  $\pm 10\%$  of the expected values. The exception is the *z*-band throughput, which is 20% low, likely due to an underestimate of the QE dropoff at red wavelengths.

The band passes for the filters alone, and for the complete system, including atmosphere, are shown in Figure 12. A feature that we discovered with the MMT Megacam *g* filter was the presence of a noticeable radial and time-variable gradient in the background level after the images were flattened. This filter has a slight shift in the red-end cutoff wavelength from center to corner, which is very close to the atomic oxygen airglow line at 5577 Å. Thus, when we purchased the Magellan filter we chose to shift the red-end cutoff further blueward to avoid this line.

In addition to the standard *ugriz* filter sets, observers have purchased specialized filters for their programs, including narrow-band filters. Some of these filters have been constructed from four 150 mm<sup>2</sup> pieces. This construction reduces cost, but at the expense of needing to mask the gaps in the filters causing partial vignetting in a “plus sign” shape across the mosaic.

### 8.2. Photometry

In principle, the photometric precision that can be obtained will be limited by photon counts from the object itself or from the underlying sky. For short exposures or with narrowband filters, there may be an additional contribution due to the detector read-noise.

In practice, how close one gets to the theoretical limit is limited by considerations of where the object falls on the mosaic, the underlying spectrum of the object, and how bright the object is.

#### 8.2.1. Time-series Photometry

The best precision is obtained for time-series photometry where one is interested primarily in how stable a particular object is. A detailed analysis of time-series photometry with Megacam was performed by Hartman et al. (2005). They showed that with  $\approx 60$  s exposures, the photon limit can be achieved for point sources with  $16 < r < 24$  by performing image subtraction and then point-spread function-fitting the residuals. For brighter objects, image subtraction followed by aperture photometry allows photon-limited performance at brighter magnitudes with a maximum precision of 0.36 mmag.

#### 8.2.2. Chip-to-Chip Variations

If one is instead interested in the relative brightness of objects distributed across the full field-of-view, the precision will not reach the photon limit. By using the data used to determine the illumination correction, we can compare multiple observations of the same star made in many locations in the mosaic. For bright stars, the rms variation is typically 0.005 mag.

#### 8.2.3. Color Transformations to SDSS and CFHT

Observations of the CFHT Legacy Survey field D4 (Gwyn 2012) are used to compute approximate color transformations between the Magellan filters and the CFHT system. We find the following relations:

TABLE 3  
MEGACAM BANDPASS CHARACTERISTICS

Filter	50% Cuton (Å)	50% Cutoff (Å)	Mean filter transmission	QE	Measured total throughput	Dark sky background (mag arcsec <sup>-2</sup> )
MMT <i>u</i>	3386	3824	0.70	0.51	0.15	22.4
MMT <i>g</i>	4115	5493	0.85	0.86	0.39	21.9
MMT <i>r</i>	5673	7112	0.84	0.84	0.39	20.9
MMT <i>i</i>	7060	8723	0.88	0.55	0.25	19.8
MMT <i>z</i>	8380	9692	0.91	0.29	0.13	18.7
Magellan <i>u</i>	3416	3877	0.60	0.53	0.18	22.6
Magellan <i>g</i>	3872	5256	0.77	0.81	0.42	22.4
Magellan <i>r</i>	5602	7113	0.89	0.85	0.50	21.2
Magellan <i>i</i>	7223	8655	0.90	0.54	0.37	20.3
Magellan <i>z</i>	8355	9696	0.91	0.29	0.16	19.4

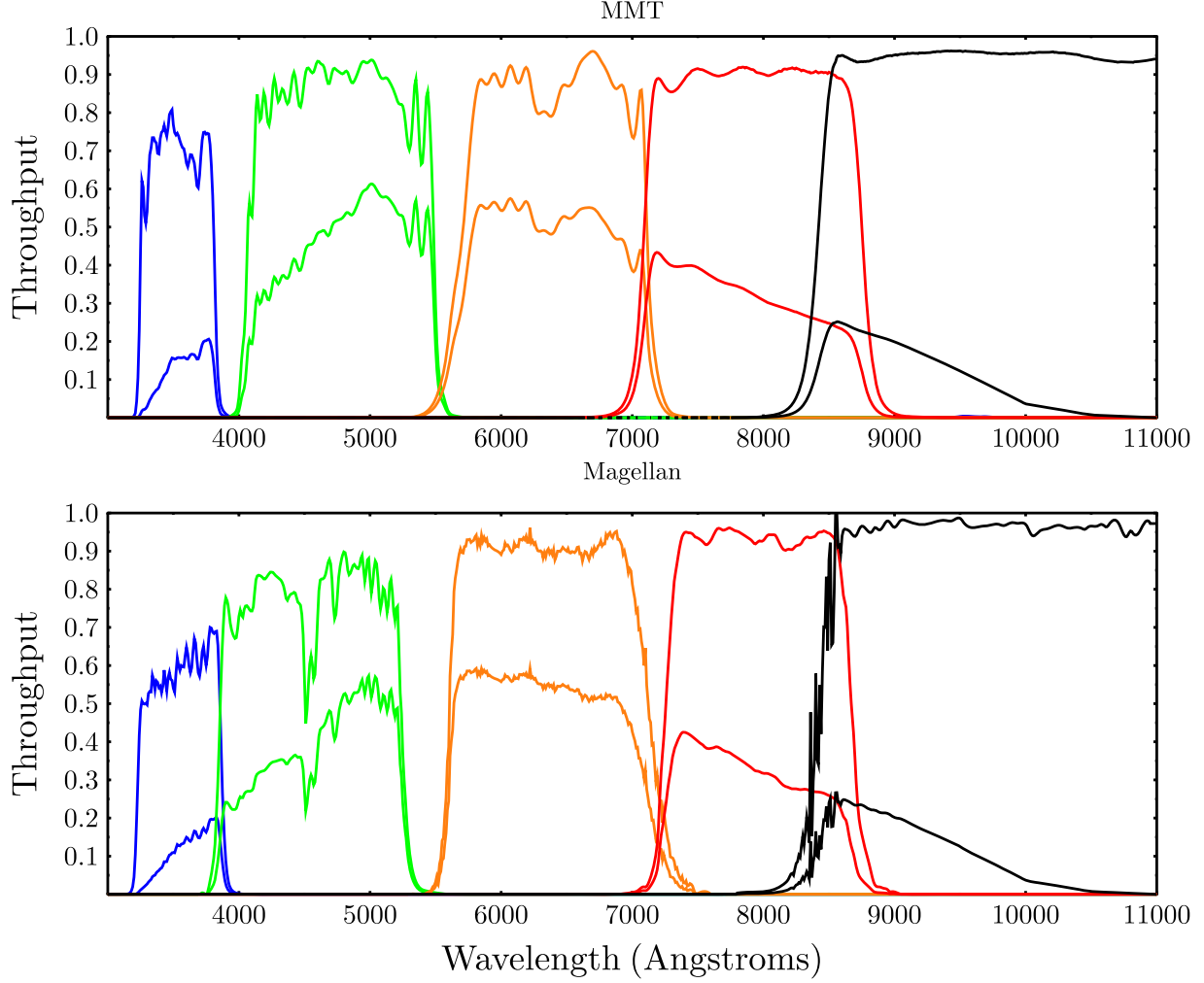


FIG. 12.—Transmission functions for the Megacam filters at MMT and Magellan. *Upper curves* are for the filter alone; lower curves are for the complete system from atmosphere to detector. See the online edition of the *PASP* for a color version of this figure.

$$u_{\text{CFHT}} = u_{\text{Mag}} - 0.30(u - g)_{\text{CFHT}}$$

$$u_{\text{SDSS}} = u_{\text{Mag}} - 0.02(u - g)_{\text{SDSS}}$$

$$g_{\text{CFHT}} = g_{\text{Mag}} - 0.33(g - r)_{\text{CFHT}}$$

$$g_{\text{SDSS}} = g_{\text{Mag}} - 0.12(g - r)_{\text{SDSS}}$$

$$r_{\text{CFHT}} = r_{\text{Mag}} + 0.05(g - r)_{\text{CFHT}}$$

$$r_{\text{SDSS}} = r_{\text{Mag}} + 0.03(g - r)_{\text{SDSS}}$$

$$r_{\text{CFHT}} = r_{\text{Mag}} + 0.05(r - i)_{\text{CFHT}}$$

$$r_{\text{SDSS}} = r_{\text{Mag}} + 0.02(r - i)_{\text{SDSS}}$$

$$i_{\text{CFHT}} = i_{\text{Mag}} - 0.01(r - i)_{\text{CFHT}}$$

$$i_{\text{SDSS}} = i_{\text{Mag}} + 0.09(r - i)_{\text{SDSS}}$$

$$i_{\text{CFHT}} = i_{\text{Mag}} - 0.03(i - z)_{\text{CFHT}}$$

$$i_{\text{SDSS}} = i_{\text{Mag}} - 0.06(i - z)_{\text{SDSS}}$$

$$z_{\text{CFHT}} = z_{\text{Mag}} + 0.07(i - z)_{\text{CFHT}}$$

$$z_{\text{SDSS}} = z_{\text{Mag}} + 0.04(i - z)_{\text{SDSS}}$$

Applying the CFHT-to-SDSS transformations in Gwyn (2012), we arrive at the following:

The estimated uncertainty in the coefficients is 0.03 for  $g$ ,  $r$ , and  $i$ , and 0.05 for  $u$  and  $z$ .

### 8.3. Astrometry

When solving for the chip locations and distortion, the typical variation in the position of each star among the several dithered exposures is 6 mas.

The standard observing and reduction procedure has all of the astrometric exposures taken using the same position angle. A final check of the self-consistency is to take an exposure of the same field, rotated by  $90^\circ$ . We find that there is a large-scale variation with peak-to-peak amplitude of 30 mas. This is attributed to the fact that the distortion pattern is assumed to be centered exactly at the center of the mosaic, when in fact it is displaced by a few arcseconds. By adding the distortion center as a free parameter to the fit, we expect to reduce significantly this source of error in the global astrometric solution.

We evaluate the stability of the astrometric solution on a timescale of days by comparing exposures of the same field taken over a period of 5 days. The rms stability of the individual position measurements of each star relative to its mean position is 11 mas.

Figure 13 shows the scatter in the separation of pairs of stars taken over a one week observing period. For each of a set of 10,000 pairs of stars, we compute the vector difference in their positions and subtract it from the individual vector differences. The quantity plotted is the rms length of the residual vectors, averaged into bins of  $15''$  separation.

Typical residuals to the 2MASS catalog are 120 mas, which are dominated by the errors in the 2MASS catalog (Skrutskie et al. 2006).

### 8.4. Image Quality

The dominant contributor to the FWHM of the images recorded by Megacam is the atmosphere, even in the best seeing conditions, which at Magellan is occasionally as good as  $0.3''$  FWHM in  $r$ -band. Contributions from the nominal telescope and corrector, and from residual aberrations have been discussed above. Additional contributors are discussed in the following sections.

#### 8.4.1. Chromatic Elongation from the Atmosphere

Because there is no atmospheric dispersion corrector, images taken off-zenith will be elongated in the elevation direction. The amount of expected elongation can be computed using the atmospheric refraction function (Wallace 2005), combined with the filter transmission functions. The ellipticity follows the form  $e \equiv 1 - b/a$  and is  $e_0[\tan(z)/\text{FWHM}]^2$ , at a zenith distance  $z$ , and seeing is in arcseconds, where  $e_0 = [0.016, 0.047, 0.011, 0.003, 0.0004]$ , computed from the *ugriz* system bandpasses. For example, a  $g$ -band exposure taken  $30^\circ$  off zenith in  $0.5''$  seeing will have an ellipticity of 0.06.

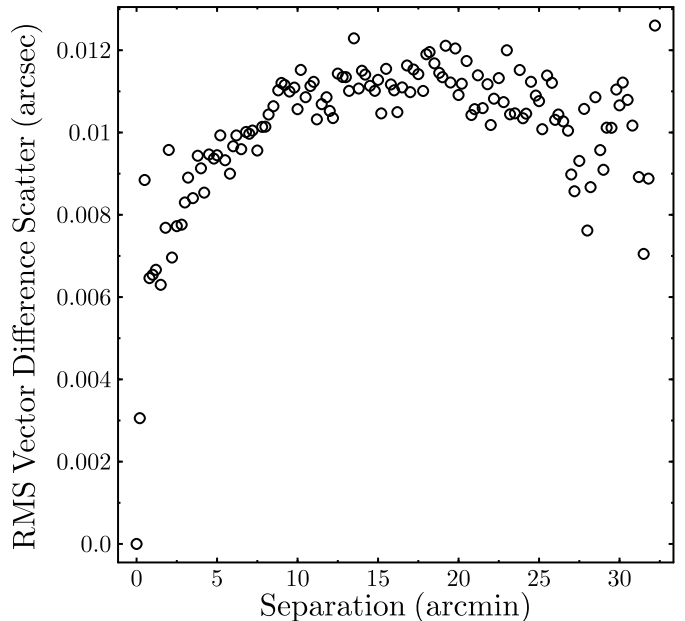


FIG. 13.—Scatter in position vectors between pairs of stars as a function of distance.

#### 8.4.2. Miscollimation

Because full field wavefront sensing is normally performed only at the beginning of each run (see § 6.2), there is some residual field-dependent astigmatism. This contributes to the ellipticity at a level of 0.02.

#### 8.4.3. Distortion

As discussed in the astrometry section above, the distortion pattern is represented as a radial polynomial. A round image will be stretched radially, so that the tangential to radial axis ratio  $b/a = (dr/d\theta)/(r/\theta)$ , or  $e \approx -2PV_2\theta^2 + 4PV_5\theta^4$ . At the corners of the Megacam field  $e = 0.018$ .

#### 8.4.4. Observed Ellipticity

After accounting for the above sources, there typically remains a few percent residual ellipticity. The source of the ellipticity is not currently understood, but can be mitigated by fitting polynomials to the ellipticity components when performing weak lensing analysis.

### 8.5. Scientific Samples

#### 8.5.1. Weak Lensing

Several groups have undertaken weak lensing studies with Megacam. The first, by Israel et al. (2012), looked at seven X-ray selected clusters with  $0.35 < z < 0.9$ . In a comparison with CFHT data, they found a high level of consistency in the lensing signal for CL1701+6414 and concluded that

Megacam is suitable for weak lensing studies. Subsequent analysis (Israel et al. 2014) determined that the masses determined by weak lensing and by X-ray observations are consistent.

High et al. (2012) observed a sample of clusters from the South Pole Telescope survey with the goal of comparing their masses with those derived from the Sunyaev-Zel'dovich effect and from X-ray measurements. They find statistical consistency at the 20% level.

In an attempt to measure cluster galaxy halo truncation, Levinson (2014) measured the flexion of background galaxies behind Abell 1689. The Megacam measurements revealed that the background galaxies at  $z \sim 1$  had intrinsically larger shape noise than expected. This prevented a determination of the halo truncation in the foreground lensing galaxies.

### 8.5.2. Satellite Galaxies

In the northern hemisphere, there have been several strikingly successful programs attempting to find faint dwarf companions to the Galaxy and also our nearest large neighbor, M31. Belokurov et al. (2007) and Zucker et al. (2007) have used data from SDSS, while McConnachie & PAndAS Collaboration (2012) have targeted the environs of M31 and M33 with the PAndAS survey using the CFHT and its own MegaCam. Both groups used pipeline-produced stellar photometry in more than one band to search for color–magnitude features such as the red giant branch. The PAndAS data, in particular, was quite deep, detecting stars down to the level of the horizontal branch at M31. A group is now using Megacam to search for similar dwarfs around two southern galaxies—a more difficult task given the greater distances. The two galaxies being surveyed are NGC 253, part of the Sculptor Group, at a distance of 3.3 Mpc, and NGC 5128, part of the Cen A group, at a distance of 3.8 Mpc.

Previous wide-field surveys for satellite galaxies in NGC 253 used photographic material to search for unresolved galaxy light (e.g., Cote et al. 1997 ; Jerjen et al. 2000). Of their sample of dwarfs, none were fainter than  $M_V = -9$ , and the survey was already incomplete at  $M_V = -14$ . With Megacam, a complete survey out to a radius of 75 kpc, and down to  $M_V = -9$  is possible for both these dwarfs by obtaining stellar photometry

down to  $r = 26.5$ . As many as six new satellite galaxies could be discovered in the NGC253 area, assuming that its satellite system has the same properties as M31. So far, one new dwarf has been found in the NGC 253 data (Sand et al. 2014). For NGC 5128, good coverage out to 50 kpc has been obtained, and the survey is continuing out to a radius of 150 kpc. A paper reporting the discovery of two new NGC 5128 dwarfs has been published Crnojević et al. (2014), and *Hubble Space Telescope (HST)* time to follow up the discoveries with deeper photometry has been secured.

### 8.5.3. Solar System Searches

Megacam was used extensively in the ground-based portion of the search for faint Kuiper Belt objects that the *New Horizons* spacecraft could reach after its encounter with the Pluto and Charon. Megacam at Magellan was particularly well-suited to this task because a large area near the intersection of the galactic and ecliptic planes needed to be searched. The excellent image quality that can be achieved with the Megacam/Magellan combination helped to overcome issues of stellar crowding, as well as to reach magnitudes fainter than  $r \sim 26$ . While the secondary targets for *New Horizons* are even fainter and required the use of *HST* to discover, the Megacam images can be used to extend the orbital arcs of those targets. The Megacam search yielded the discovery of a new Neptune Trojan (Parker et al. 2013) and identified targets that will be examined at long range with *New Horizons* (Benecchi et al. 2015). The Megacam search data, in combination with the *HST* data, will also be used in refining our understanding of the size distribution of small Kuiper belt objects.

Funding for Megacam was provided through the Major Scientific Instrumentation fund of the Smithsonian Institution and the Harvard College Observatory. Observations reported here were obtained at the MMT Observatory, a joint facility of the Smithsonian Institution and the University of Arizona. This paper includes data gathered with the 6.5 m Magellan Telescopes located at Las Campanas Observatory, Chile.

*Facilities:* MMT (Megacam imager), Magellan:Clay (Megacam imager).

## REFERENCES

- Belokurov, V., et al. 2007, *ApJ*, 654, 897  
 Benecchi, S. D., et al. 2015, *Icarus*, 246, 369  
 Bertin, E., & Arnouts, S. 1996, *A&AS*, 117, 393  
 Bertin, E., et al. 2002, in *ASP Conf. Ser.* 281, *Astronomical Data Analysis Software and Systems XI*, ed. D. A. Bohlender, D. Durand, & T. H. Handley (San Francisco: ASP), 228  
 Bianco, F. B., Protopapas, P., McLeod, B. A., Alcock, C. R., Holman, M. J., & Lehner, M. J. 2009, *AJ*, 138, 568  
 Boulade, O., et al. 2003, *Proc. SPIE*, 4841, 72  
 Calabretta, M. R., & Greisen, E. W. 2002, *A&A*, 395, 1077  
 Callahan, S., Caldwell, N., Williams, G. G., Chute, C., & Pickering, T. E. 2008, *Proc. SPIE*, 7018, 701843  
 Cote, S., Freeman, K. C., Carignan, C., & Quinn, P. J. 1997, *AJ*, 114, 1313  
 Crnojević, D., et al. 2014, *ApJ*, 795, L L35  
 Fabricant, D., et al. 2004, *Proc. SPIE*, 5492, 767  
 Fata, R. G., & Fabricant, D. G. 1998, *Proc. SPIE*, 3355, 275  
 Flaugher, B. L., et al. 2012, *Proc. SPIE*, 8446, 844611  
 Gwyn, S. D. J. 2012, *AJ*, 143, 38  
 Hartman, J. D., et al. 2005, *AJ*, 130, 2241  
 Hartman, J. D., et al. 2008, *ApJ*, 675, 1233



- High, F. W., et al. 2012, *ApJ*, 758, 68
- Israel, H., et al. 2012, *A&A*, 546, A 79
- . 2014, *A&A*, 564, A 129
- Jerjen, H., Binggeli, B., & Freeman, K. C. 2000, *AJ*, 119, 593
- Joye, W. 2011, in *ASP Conf. Ser. 442, Astronomical Data Analysis Software and Systems XX*, ed. I. N. Evans, A. Accomazzi, D. J. Mink, & A. H. Rots (San Francisco: ASP), 633
- Kahn, S. M., et al. 2010, *Proc. SPIE*, 7735, 77350J
- Lasker, B. M., et al. 2008, *AJ*, 136, 735
- Levinson, R. S. 2014, Ph.D. thesis, MIT, Cambridge, MA
- McConnachie, A. W., & PAndAS Collaboration 2012, in *ASP Conf. Ser. 458*, ed. W. Aoki (San Francisco: ASP), 271
- McLeod, B. A. 1996, *PASP*, 108, 217
- McLeod, B., et al. 2006, *Scientific Detectors for Astronomy 2005*, eds. J. Beletic, J. Beletic, & P. Amico (Dordrecht, The Netherlands: Springer), 337
- Miyazaki, S., et al. 2002, *PASJ*, 54, 833
- . 2006, *Proc. SPIE*, 6269, 62690B
- Onaka, P., et al. 2012, *Proc. SPIE*, 8453, 84530K
- Parker, A. H., et al. 2013, *AJ*, 145, 96
- Pickering, T. E., West, S. C., & Fabricant, D. G. 2004, *Proc. SPIE*, 5489, 1041
- Rockosi, C. M., Gunn, J. E., Carr, M. A., et al. 2002, *Proc. SPIE*, 4836, 180
- Roll, J. B., & Mandel, J. 2001, in *ASP Conf. Ser. 238, Astronomical Data Analysis Software and Systems X*, ed. F. R. Harnden, F. A. Primini Jr., & H. E. Payne (San Francisco: ASP), 233
- Sand, D. J., et al. 2014, *ApJ*, 793, L7
- Schaller, S. 1990, in *ASP Conf. Ser. 8, CCDs in Astronomy*, ed. G. H. Jacoby (San Francisco: ASP), 206
- Schechter, P. L., Burley, G. S., Hull, C. L., Johns, M., Martin, H. M., Schaller, S., Shectman, S. A., & West, S. C. 2003, *Proc. SPIE*, 4837, 619
- Skrutskie, M. F., et al. 2006, *AJ*, 131, 1163
- Szentgyorgyi, A., et al. 2012, *Proc. SPIE*, 8446,
- van Dokkum, P. G. 2001, *PASP*, 113, 1420
- Wallace, P. T. 2005, *SLALIB Positional Astronomy Library, Starlink User Note 67* (Oxfordshire, UK: Rutherford Appleton Laboratory)
- Wittman, D. M., et al. 1998, *Proc. SPIE*, 3355, 626
- Zucker, D. B., et al. 2007, *ApJ*, 659, L 21